Contrib Mineral Petrol (2014) 167:1010
DOI 10.1007/s00410-014-1010-x

ORIGINAL PAPER

A re-examination of petrogenesis and $^{40}Ar/^{39}Ar$ systematics in the Chain of Ponds K-feldspar: "diffusion domain" archetype versus polyphase hygrochronology

Alex N. Chafe · Igor M. Villa · John M. Hanchar · Richard Wirth

Received: 14 January 2014 / Accepted: 19 April 2014 / Published online: 6 May 2014

Abstract K-feldspar (Kfs) from the Chain of Ponds Pluton (CPP) is the archetypal reference material, upon which thermochronological modeling of Ar diffusion in discrete "domains" was founded. We re-examine the CPP Kfs using cathodoluminescence and back-scattered electron imaging, transmission electron microscopy, and electron probe microanalysis. $^{40}Ar/^{39}Ar$ stepwise heating experiments on different sieve fractions, and on handpicked and unpicked aliquots, are compared. Our results reproduce the staircase-shaped age spectrum and the Arrhenius trajectory of the literature sample, confirming that samples collected from the same locality have an identical Ar isotope record. Even the most pristine-looking Kfs from the CPP contains successive generations of secondary, metasomatic/retrograde mineral replacements that post-date magmatic crystallization. These chemically and chronologically distinct phases are responsible for its staircase-shaped age spectra, which are modified by handpicking. While genuine within-grain diffusion gradients are not ruled out by these data, this study demonstrates that the most important control on staircase-shaped age spectra is the simultaneous presence of heterochemical, diachronous post-magmatic mineral growth. At least five distinct mineral species were identified in the Kfs separate, three of which can be traced to external fluids interacting with the CPP in a chemically open system. Sieve fractions have size-shifted Arrhenius trajectories, negating the existence of the smallest "diffusion domains." Heterochemical phases also play an important role in producing nonlinear trajectories. In vacuo degassing rates recovered from Arrhenius plots are neither related to true Fick's Law diffusion nor to the staircase shape of the age spectra. The CPP Kfs used to define the "diffusion domain" model demonstrates the predominance of metasomatic alteration by hydrothermal fluids and recrystallization in establishing the natural Ar distribution among different coexisting phases that gives rise to the staircase-shaped age spectrum. Microbeam imaging of textures is as essential for $^{40}Ar/^{39}Ar$ hygrochronology as it is for U–Pb geochronology.

Keywords Hygrochronology · K-feldspar geochronology · Cathodoluminescence · Electron probe microanalysis · $^{40}Ar/^{39}Ar$ age spectra · Arrhenius trajectories

Communicated by J. Hoefs.

Electronic supplementary material The online version of this article (doi:10.1007/s00410-014-1010-x) contains supplementary material, which is available to authorized users.

A. N. Chafe · J. M. Hanchar
Earth Sciences Department, Memorial University of Newfoundland, St. John's, NL A1B 3X5, Canada
e-mail: a.chafe@mun.ca

J. M. Hanchar
e-mail: jhanchar@mun.ca

I. M. Villa (✉)
CUDAM, Università di Milano Bicocca, 20126 Milan, Italy
e-mail: igor@geo.unibe.ch

I. M. Villa
Institut für Geologie, Universität Bern, Baltzerstrasse 3, 3012 Bern, Switzerland

R. Wirth
3.3, Helmholtz Centre Potsdam, GFZ German Research Centre for Geosciences, 14473 Potsdam, Germany
e-mail: wirth@gfz-potsdam.de

Introduction

The debate whether mineral ages are controlled exclusively by ambient temperature or are principally influenced by fluid-induced recrystallization is half a century old (e.g., Tilton 1960; Jäger 1962; Arnold and Jäger 1965; Chopin and Maluski 1980). For most isotope systems in most minerals (e.g., U–Pb, Rb–Sr and K–Ar in zircon, monazite, biotite, white mica.), the ubiquitous observations of patchy intra-crystalline age zoning patterns and the scarcity of observations of bell-shaped diffusion profiles have made it clear that in most cases, diffusion has played a subordinate role in the establishment of the isotope record of a mineral (Villa and Williams 2013). The agreement of Goldich's (1938) weathering series with the typical mineral age sequence (zircon > amphibole > feldspars) implies that the true control on isotope exchange is provided by the average interatomic bond length/strength (Dahl 1997), but gives no guarantee on whether these bonds were broken by temperature, fluids, deformation, or a non-unique combination of all three factors (Villa 2006), preventing an unambiguous reconstruction of paleotemperatures. In fact, a fundamental observation is that metasomatic fluids are responsible for more efficient isotope mobility than temperature (Cole et al. 1983; Lasaga 1986).

An apparent exception to this general rule is a single mineral; K-feldspar (Kfs) and a single isotope system, K–Ar (Lovera et al. 1993). While there is abundant laboratory data on Ar diffusion in gem-quality Kfs under controlled conditions (Foland 1994, Wartho et al. 1999, and references therein), the applicability of the gem experiments to complex natural samples has not been unambiguously documented. In the early days of K–Ar geochronology (e.g., Hart 1964), it was thought that as the chemical properties of Ar do not allow it to bond with other elements in a mineral structure, the Ar mobility in and out of mineral structures was extremely high (proof of the contrary was quantitatively provided much later by Nyfeler et al. (1998), who linked Ar mobility to Si,Al exchange in Kfs). Furthermore, Kfs mineral ages were normally the youngest of any given suite of minerals dated in a sample, e.g., the contact-metamorphic traverse studied by Hart (1964). Unfortunately, as Hart (1964) did not consider that fluids are exsolved from the solidifying magma into its contact-metamorphic aureole (the very cause of porphyry ore deposits), the paradigm of Kfs as undergoing only thermally induced, "dry" diffusive ^{40}Ar loss has been entrenched in the minds of many geologists ever since.

Parsons et al. (1988) investigated the phenomenon of ^{40}Ar loss in Kfs by correlating age data with transmission electron microscope (TEM) microstructural observations. They identified a number of incoherent boundaries within the Kfs crystals either related to primary crystallization and perthitization, or to post-crystallization metasomatic alteration, turbidity, and unit cell dislocations. They extensively imaged and degassed a variety of Kfs structural and chemical states, concluding that turbidity was the best indicator of ^{40}Ar loss. Parsons et al. (1988) also pointed out that turbidity is a common textural property of Kfs in all but young and fresh volcanic samples; in optical microscopy, turbidity is the mineral-defining characteristic. If turbidity leads to ^{40}Ar loss and turbidity is due to deuteric fluids that have interacted with the feldspars (Worden et al. 1990; Parsons et al. 1999), then this implies that the principal factor controlling K–Ar ages is the reaction with fluids. The question is not only at what temperature the reactions occurred, but also whether the fluids were of external origin. If metasomatic alteration and recrystallization occur as separate events in a sample's retrogression history, then they have no unique causal link with the ambient temperature.

Using a different approach, Lovera et al. (1993) examined the ^{39}Ar release kinetics of Kfs samples in vacuo. They plotted the bulk degassing rate obtained from a step-heating experiment, D/a^2 (where D is the diffusion coefficient and a has the dimension of a length) on an Arrhenius diagram as a function of inverse temperature. They obtained curved trajectories. Such curvatures can be either extrinsic, being the effect of a perfectly linear D modulated by a variable geometric factor, a (Lovera et al. 1993), or intrinsic, being due to nonlinear Arrhenian behavior inherent in D (Villa 2013; Cassata and Renne 2013, Fig. 8). The crucial role is that of a: if the curvature of the Arrhenian trajectories is an intrinsic property of D, then a represents the size of the degassing grain and is constant, but if D is assumed to be rigorously linear, then all of the nonlinearity must be taken up by variations of a, which becomes a strictly geometric factor identifying the effective grain size of "domains" making up the Kfs structure.

Attempts to physically identify these Ar "diffusion domains" by TEM have not been successful (Fitz Gerald and Harrison 1993, p. 377; Waldron et al. 1994; Lee et al. 1995; Lee and Parsons 1997; Fitz Gerald et al. 2006; Parsons et al. 2009, 2010, 2013). Moreover, the physical reality of recoil (Huneke and Smith 1976) forbids the existence of resolvable "domains" smaller than ca. 0.1 μm (Onstott et al. 1995; Villa 1997). Even more important than the external inconsistencies are the internal ones; the example of literature Kfs samples modeled with "diffusion domains" and recalculated by Villa (2006) showed that the modeled Kfs fails to obey the diffusion equations for isothermal step heating. Moreover, the modeled thermal histories require that there was no thermal equilibration between neighboring samples (Villa 2006, p. 170–171). The bulk of independent geological evidence thus appears to expose internal inconsistencies in "domain" modeling of Kfs data.

The Chain of Ponds Pluton (CPP) sample MH-10 (Heizler et al. 1988) was the archetype Kfs, on which the "diffusion domain" modeling was based (Lovera et al. 1993; Fitz Gerald and Harrison 1993). The present study reports a re-examination of a freshly collected sample of the CPP Kfs at the exact sampling locality of sample MH-10 (Fig. S1; Appendix I; D. Lux, pers. comm.) and given the sample name CPP-02-01. The collected sample is as close to scientific reproducibility as any natural rock sample can be. The present study proposes a more extensive context for the interpretation of $^{40}Ar/^{39}Ar$ data on the basis of the recent advances in the comprehension both of Kfs as a geochronometer (Villa et al. 2006) and of the petrogenesis and subsequent metasomatic alteration of Kfs (Villa and Hanchar 2013). The Kfs mineral chemistry was obtained from electron probe microanalysis (EPMA) and analytical TEM combined with imaging by cathodoluminescence (CL), back-scattered electron (BSE) and TEM. We will demonstrate that these analyses and imaging techniques reveal that the Kfs grains analyzed contain separate multiple feldspar phases that are chemically and chronologically distinct, that the heterochemical phases identified by micro-imaging can be easily recognized using Ar isotope systematics, and that they can be physically separated by handpicking. An improved characterization of the CPP sample enabled us to ascertain the factors controlling Ar systematics in Kfs. This insight needs to be taken into consideration when interpreting all $^{40}Ar/^{39}Ar$ analyses.

Results

Sampling locality and analytical methods are described in detail in Online Supplement text file Appendix I.

Petrography

The rock sample CPP-02-01 is medium coarse-grained, consisting of mostly subhedral grains dominated by plagioclase feldspar with lesser amounts of Kfs, quartz, biotite, and hornblende. Examination with a hand lens suggests post-emplacement alteration with a dull white "chalky" appearance to the feldspars in hand sample. Petrographic examination of thin sections using cross-polarized light (XPL) optical microscopy reveals that the plagioclase is sericitized throughout the majority of the grains, especially along fractures and at grain boundaries, and shows coarse lamellar twinning throughout. The plagioclase also contains relatively fresh unaltered patches in many of the grains. Kfs contains fresh regions with no evidence of alteration; however, it also contains regions (typically along fractures and at grain boundaries) that are extensively altered (Fig. 1a, c). Quartz occurs in a bimodal grain size: coarser grains around 1 mm and very fine, $\ll$1 mm agglomerates. Biotite and hornblende are the primary mafic phases in CPP-02-01. Biotite, which is partially replaced by chlorite in some grains, occurs as aggregates up to 2 mm in diameter.

Accessory phases include titanite, apatite, zircon, and carbonate. With the exception of carbonate (which is predominately anhedral and fills fractures), all of the accessory phases are fine grained and euhedral. The apatite and zircon are nearly exclusively contained in biotite, whereas the titanite typically occurs at grain boundaries.

Cathodoluminescence/BSE imaging and electron probe microanalysis

The different Kfs generations were identified and further examined using CL and BSE (Fig. 1) followed by EPMA (Fig. 2). Both plagioclase and Kfs luminesce in bright and dark shades of green and blue, respectively. CL imaging also found small inclusions of Kfs within plagioclase and quartz that were overlooked using traditional optical microscope petrography. These crystals are significantly smaller than others in the sample and are bounded by either plagioclase or quartz. Even crystals that appear nearly pristine under the optical microscope show CL intensity variations.

We acquired three EPMA traverses selected to cover zones having different CL behavior. Data are presented in Table S1; the location maps are shown in Fig. 1a, e. Traverse C–C′ is from a "pristine"-looking grain in CL; A–A′ was acquired in a porous, turbid zone with murky CL emissions; B–B′ was acquired across two plagioclase-Kfs boundaries, to examine to what extent the grain boundaries acted as fast pathways for fluids that infiltrated the sample. The chemical composition of the Kfs and the distribution of bright/dull CL emitting patches are strongly variable in the two traversed grains.

Transmission electron microscopy

Transmission electron microscopy observations were made in two areas of the CPP-02-01 Kfs, selected on the basis of the CL and BSE images in Figs. 1a and 3a. Focused ion beam (FIB) TEM foil 1 imaged uniform Kfs from a pristine area in the sample, which shows minor microcline twinning, but is otherwise homogenous and relatively unaltered. In contrast, TEM foil 2 (Fig. 3b) is highly complex; it shows fluid pathways, dissolution fronts at the Kfs-plagioclase boundary, and a Ba-rich vein. The spots analyzed using energy dispersive X-ray analysis (EDAX) by analytical TEM are located at the bottom left of Fig. 3b, and marked on Fig. 3c. Barium enrichment within the Kfs is irregular over a distance of 200 nm (Fig. 3d, e) and appears associated with

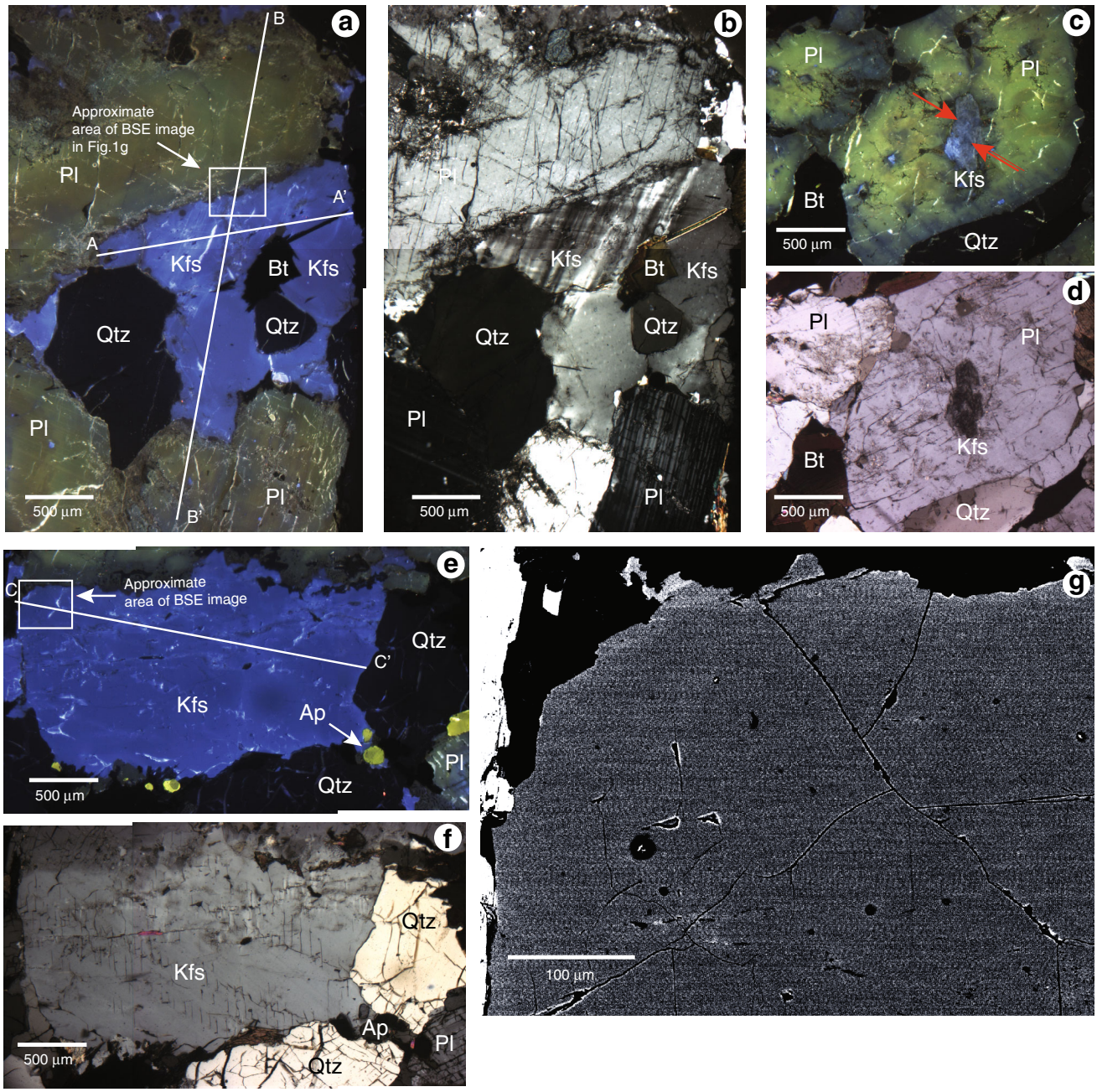

Fig. 1 Petrography of CPP-02-01. *Scale bars* in (**a**–**f**) are 0.5 mm. **a** CL photomicrograph of a region of thin section CPP-02-01. K-feldspar luminesces *blue*; *green* is plagioclase; quartz and biotite do not emit CL. Brightness of emission varies within each crystal, indicative of crystal-chemical variations. EPMA traverses A–A′ and B–B′ (Fig. 3) are shown, traverse C–C′ is in a different grain (Fig. 1e). The *rectangle* indicates the position of the BSE image in Fig. 3. **b** Optical micrograph (crossed Nicols) of the same area. **c** CL photomicrograph of a different region of thin section CPP-02-01. The wispy dendritic textures (*red arrows*) trace pathways of external fluid ingress into Kfs. **d** Optical micrograph (crossed Nicols) of the same area**. e** CL image of a "fresh" Kfs grain hosting EPMA traverse C–C′. *Bright yellow* grains at *bottom left* and *right* are apatite. The *square* locates the BSE image in Fig. 1g. **f** Optical micrograph (crossed Nicols) of the same area. **g** BSE image of a detail of the same grain; *scale bar* 0.1 mm

retrogressed regions, similar to the sample imaged by Villa and Hanchar (2013). Reactions in the Kfs resulted in microporosities; quite extensive altered regions are concentrated on the phase boundaries with albite. Kfs outside of the reaction patches visually appears more uniform and pristine.

$^{40}Ar/^{39}Ar$ analyses

Data from $^{40}Ar/^{39}Ar$ analyses obtained in this study were used to construct the age spectra and the Arrhenius and three-isotope correlation diagrams of sample CPP-02-01

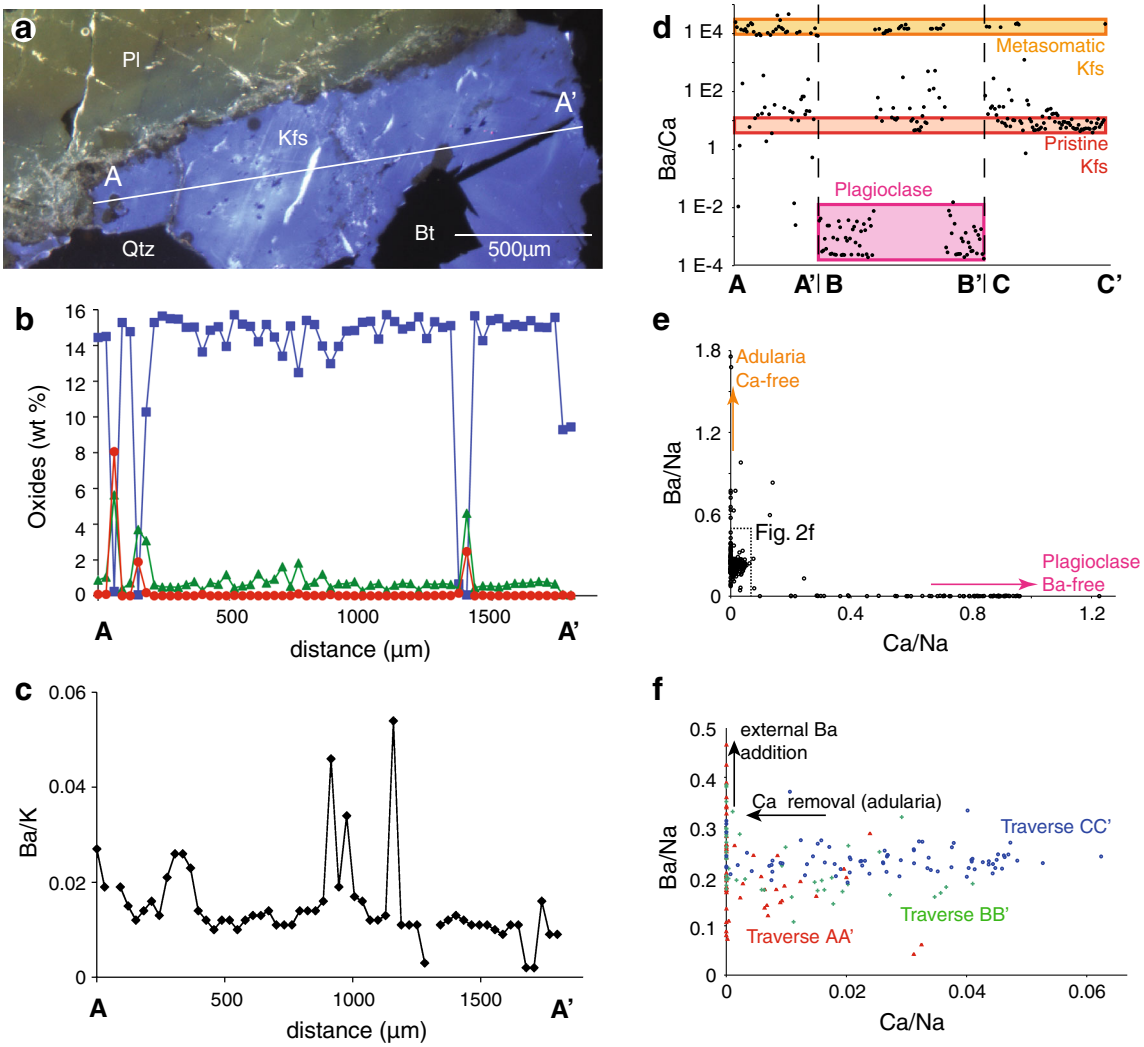

Fig. 2 EPMA traverses through plagioclase and Kfs. **a** Detail of the CL emission across EPMA traverse A–A′ in Fig. 1b. **b** Major element composition along A–A (EPMA data in Table S1). The variations are small, and show no clear correlation with the CL variations of Fig. 2a. This emphasizes the ability of CL to detect subtle petrogenetic zoning (cf. Leichmann et al. 2003) even if the major element composition remains that of Kfs. **c** Intra-grain variations of the Ba/K atom/atom ratio along A–A′. Ba, a trace element, is compatible in the Kfs structure, and its variation should be smooth in an ideal, single-stage post-magmatic cooling. Its observed irregular variations point to ingress of an external fluid, as Ba is highly soluble. **d** Intra-grain variations of the Ba/Ca atom/atom ratio in all three traverses, for a total of 270 point analyses. Data points are observed to cluster in three distinct ranges: low Ba/Ca ratios correspond to plagioclase, intermediate ones to pristine Kfs, and high ones to adularia. **e** Ba/Na vs Ca/Na (atom/atom ratios) correlation diagram of all three traverses. Plagioclase in B–B′ (green luminescence in Fig. 1a) plots at the far right of the diagram (*arrow*). The pristine Kfs in C–C′ plots in the cluster near the origin. Ba-rich adularia (*arrow*) is mostly observed in A–A′. **f** Detail of the preceding diagram. Note change of axis scales. Over 80 % of the analyses of C–C′ (*blue open circles*) plot in an elliptical cluster, with comparatively uniform Ba/Na ratios; point analyses from B–B′ (*green crosses*) are more shifted toward Ca-free compositions typical of adularia (*horizontal arrow*); the *filled red triangles* are the points from traverse A–A′, which lies close and parallel to the grain boundary, and are mostly adularia with strongly variable Ba concentrations (*vertical arrow*). The near-absence of points lying upward of the C–C′ cluster indicates that the formation of adularia occurred first, and ingress of the Ba-bearing fluid occurred later in a separate and spatially more limited event

shown in Figs. 4, 5, 6. Figure 4 shows age spectra of the handpicked and unpicked size fractions. The present age spectra all show staircase shapes, conforming to the previous $^{40}Ar/^{39}Ar$ CPP analyses by Heizler et al. (1988) and Lovera et al. (1993). At the lowermost furnace temperatures, apparent step ages are highly variable. At intermediate furnace temperatures, the age spectra show a monotonically increasing staircase shape. At high furnace temperatures, the step ages become fairly concordant. The Ca/K and Cl/K ratios calculated from the step-heating data (via ^{37}Ar, ^{38}Ar and ^{39}Ar) are shown in Fig. 5 using the common-denominator three-isotope correlation diagrams. The approach relating the Ca/Cl/K signature of the vertex points in such diagrams with distinct observable mineral

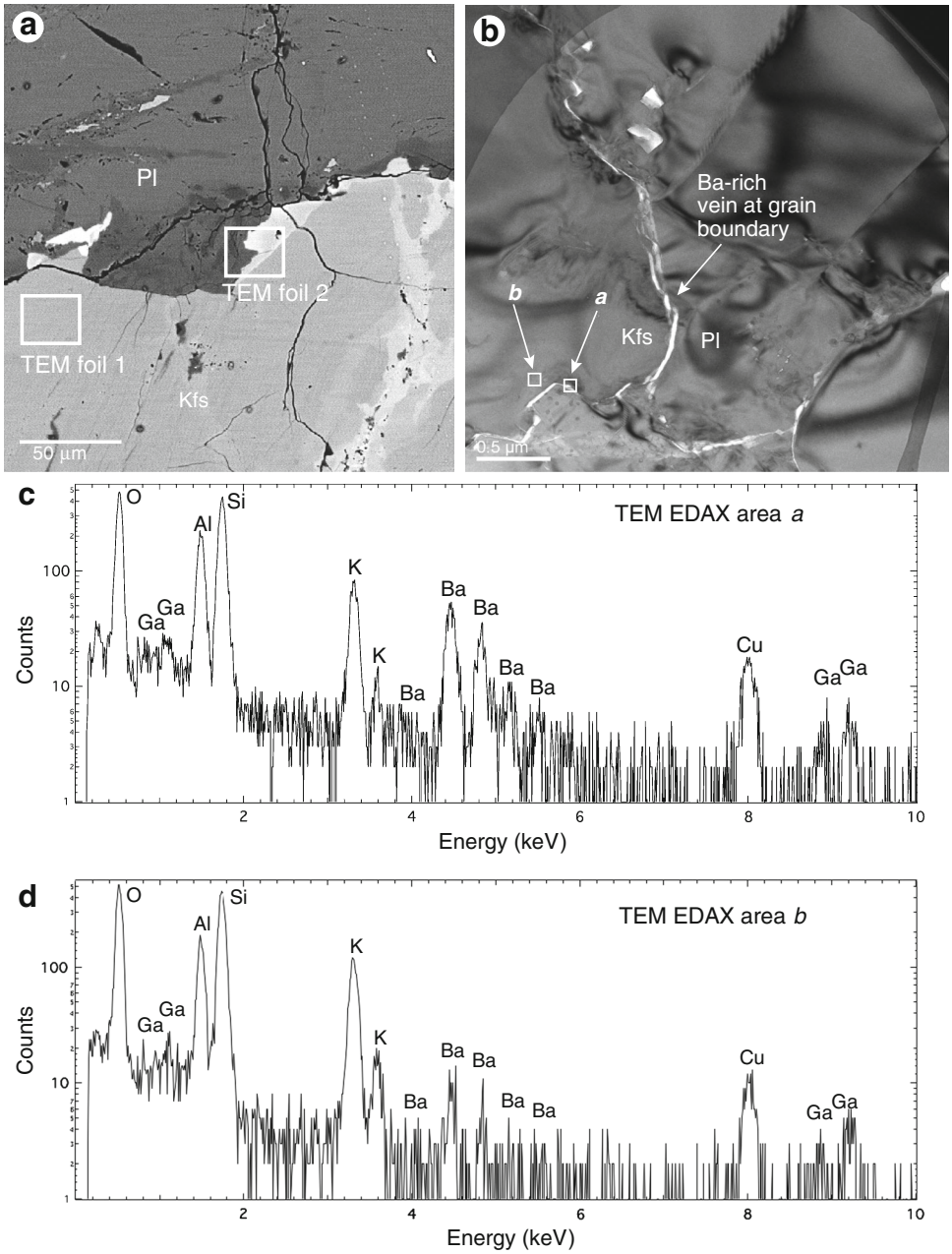

Fig. 3 TEM images and analyses. **a** Back-scattered electron location map, *scale bar* 50 µm. Two TEM foils were cut, one from location 1 in pristine Kfs (*light gray*) and one in location 2, in the middle of a zone containing several veins with different BSE contrast, at the very non-euhedral boundary with albite (*dark gray*). **b** TEM foil 2 (TEM bright-field image, *scale bar* 500 nm) showing a prominent, bright, curved vein, whose chemical analysis by TEM (*arrow a*) shows high Ba enrichment. A contiguous analysis within Kfs is marked by *arrow b*. **d, e** Quantitative EDS determination of chemical composition. *Note* the high Ba peaks only in analysis *a*. Cu is from the copper grid

phases has been validated by EPMA (Villa et al. 2000). The Arrhenius plots calculated from the ^{39}Ar release are presented in Fig. 6. The shape of the trajectories of the present samples overlaps with that of the sized fraction MH-10.s reported by Lovera et al. (1993), after correcting for a second-order effect, a horizontal shift by ca. 50 °C. As pointed out by Villa et al. (1996), the comparison between the furnace in Berne, calibrated via the melting points of pure metals, and other uncalibrated furnaces may introduce a bias in absolute temperatures, but not in the relative shape of the trajectories. For each grain size, the differences between handpicked and unpicked samples show greatest deviance at lower T. While isochroneity is not expected in a system comprised of five different phases formed at various stages during retrogression, an isochron is shown as an example (Fig. S3).

Discussion

Handpicking

As already demonstrated by Turner et al. (1971), removing some phases from a mixture changes the shape of the age spectrum. In sample CPP-02-01, purely mechanical separation (even with rigorous monitoring of heavy liquid

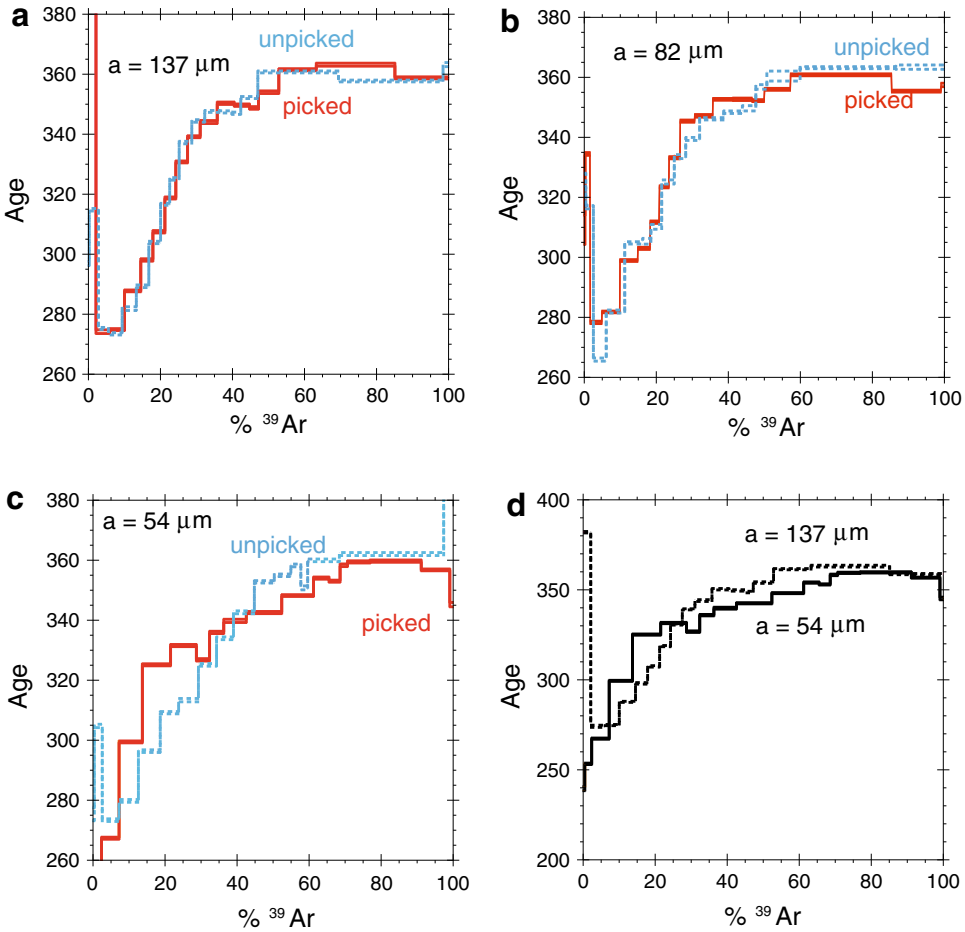

Fig. 4 Age spectra for six feldspar sieve fractions from CPP-02-01. **a** Handpicked and unpicked sieve fraction with $a = 137$ µm. *Solid red line*, handpicked; *dashed blue line*, unpicked. **b** Handpicked and unpicked sieve fraction with $a = 82$ µm. *Lines* as in Fig. 4a. **c** Handpicked and unpicked sieve fraction with $a = 54$ µm. *Lines* as in Fig. 4a. **d** Handpicked sieve fractions with $a = 137$ and 54 µm. *Solid line*, $a = 54$ µm; *dashed line*, $a = 137$ µm. The apparent age difference of high-temperature steps might be a second-order effect of diffusion, albeit superposed to a variation of the chemical composition, while the apparent age differences of low-temperature steps are incompatible with the existence of "Ar diffusion domains" proposed by Lovera et al. (1993) and are best explained by the degassing of young retrogression phases, revealed by their Ca–Cl–K signature (Fig. 5)

density) was unable to produce a pure Kfs separate. Only final handpicking achieved an improvement in Kfs purity. This is in contradiction to the purity of 99.9 % reported by Heizler et al. (1988) for their mechanical separate.

In the steps extracted at low furnace temperature, the Pirani gauge monitoring the total gas pressure in the furnace recorded a p increase by over two orders of magnitude, indicating the degassing of a hydrous phase. This was confirmed by the rapid gas clean-up time, typical of H_2O vapor. Moreover, the low-temperature steps have high Cl/K ratios and contribute a large part of the Cl budget of the sample. This effect is only weakly sensitive to handpicking, suggesting that the binocular microscope did not allow the recognition of all extraneous phases. These observations are evidence that finely inter-grown, Cl-rich alteration phases (e.g., sericite) most likely account for the low-temperature steps, which often correspond to the lowest step ages.

The high-temperature steps of the handpicked grains have lower apparent ages than the corresponding steps of the unpicked grains; the effect increases with decreasing grain size and coincides with a decrease in the Ca/K ratio in the relevant steps of the handpicked samples (Table S2). The observation that removal of plagioclase lowered the Ar*/K and Cl/K ratios is the proof that the Ar isotope record is different in plagioclase and Kfs. The higher apparent ages of plagioclase relative to Kfs can point to "parentless" (Turner 1988) ^{40}Ar. The question whether the parentless Ar has an external source (i.e., excess Ar) or an internal one (i.e., inherited Ar) is not the main concern of this study and at present has no definitive answer, as both options are plausible. It has been well documented in the literature (Villa et al. 2006 and references therein) that during crustal anatexis, feldspar minerals from the protolith can retain some Sr and Ar even at magmatic temperatures.

The effect of handpicking is even more dramatic in the chemical correlation diagrams (Fig. 5) and in the bulk chemical composition of the analyzed separate. The Ca concentrations of the three size aliquots decrease from 0.4, 0.8 and 1.6 % to 0.26, 0.23 and 0.31 %, respectively (Table S2). It must be explicitly stressed that handpicking was not designed to produce a single-generation Kfs, partly because at the time of handpicking of the present sample the full extent of the retrogression history was not even suspected. Even if some extraneous phases were removed by handpicking, the low-temperature Ar release reflects admixed phases different from Kfs.

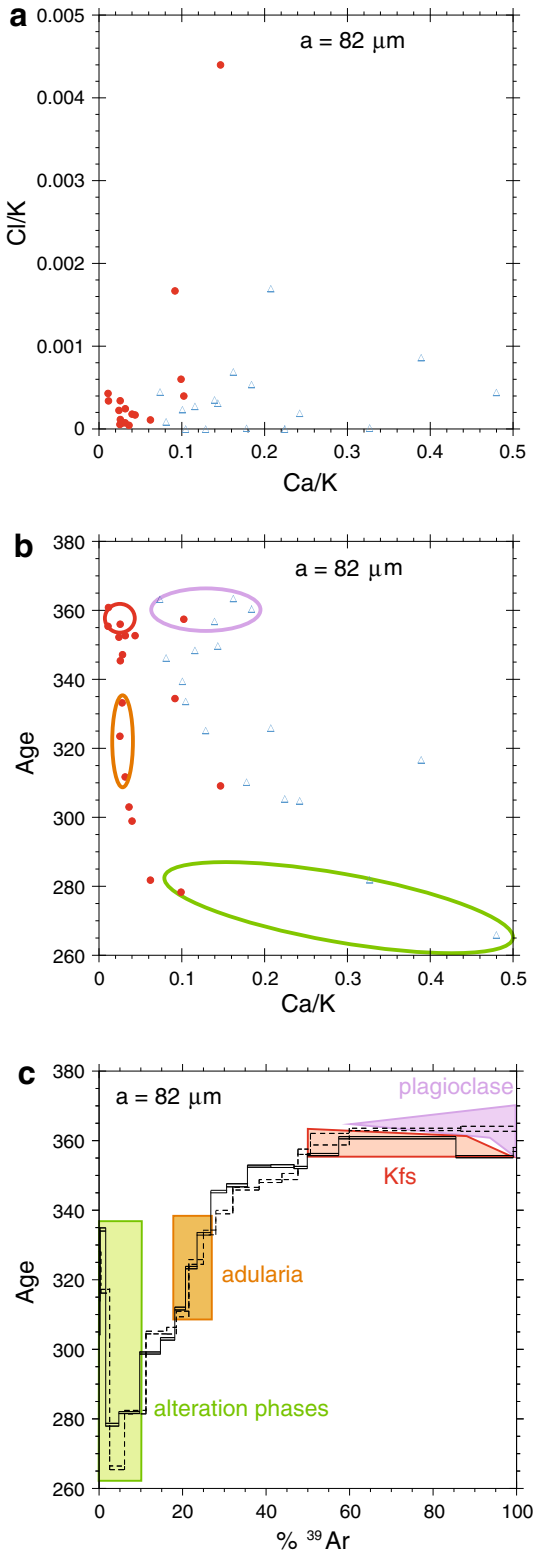

◀**Fig. 5** **a** Ca–Cl–K common-denominator three-isotope correlation diagram for handpicked sieve fraction 82 µm (*filled circles*) and for the corresponding unpicked aliquot (*open triangles*). Removing extraneous phases results in an obvious modification of the chemical signature. **b** Ca/K-age common-denominator three-isotope correlation diagram for sieve fraction 82 µm; symbols as in Fig. 5a. Removing the impurities phases by handpicking also changes the age pattern. The Ca/Cl/K signature, combined with the image analyses (Figs. 1, 2, 3), allows the straightforward identification of fields corresponding to young, Ca–Cl-rich alteration (*green*), metasomatic feldspar/adularia (*brown*), magmatic Kfs (*red*) and Ca-rich plagioclase (*mauve*). The same phase inventory is observed in all three sieve fractions, albeit in different mass proportions (see Table S2). **c** Re-interpreted age spectrum of handpicked and unpicked sieve fraction with $a = 82$ µm (from Fig. 4b). Color coding as in Fig. 5b. The phases, whose sequential degassing is fingerprinted in Fig. 5a, contribute each different step ages. Note that a full reinterpretation of the age spectrum is not possible without the constraints provided by Fig. 5a, as the age spectrum alone only contains a small part of the $^{40}Ar/^{39}Ar$ information

Petrological implications

Sample CPP-02-01 is from a road-cut outcrop, and appears at first sight as a solid, fresh rock. However, optical microscopy reveals numerous and unequivocal signs of metasomatic hydrothermal fluid infiltration and interaction. Sericitization of plagioclase, patchy replacement of Kfs, and chloritization of biotite, document the ingress of an aqueous fluid. The occurrence of secondary carbonates suggests a different episode involving H_2CO_3. These different fluid interaction episodes did not just affect the whole rock groundmass, but left clear signs in the feldspar phenocrysts. Especially germane to the status of the CPP Kfs as the archetypal thermochronometer is the sequence of successive replacement reactions. The genesis of the at least three observed Kfs generations can be explained in two mutually exclusive ways: (1) in a closed system; or (2) in a chemically open system.

Exsolution can be viewed as occurring during spinodal decomposition in a closed system. The time-scale for this microtextural evolution is <10 ka (I. Parsons, written communication 2013). It is even possible to reconcile this rapid structure formation with the occurrence of high Cl phases, as Cl is incompatible in Kfs (Smith 1974). A sort of intra-mineral differentiation could be contrived as a mechanism to repeatedly exclude any Cl initially present in the system from the successive recrystallizations and to partition it into the very last interstitial phases. Only a rapid, high-temperature, single-stage formation of the Kfs microstructures in a closed system could be reconciled with Kfs thermochronology. If all minerals having a complex grain size distribution formed in 10 ka, an age difference of 100 Ma between different domains of the Kfs must perforce record a thermal history.

The observation of a Ba-rich Kfs veinlet, however, is the decisive evidence against closed-system behavior. Unlike Cl, Ba is compatible in Kfs (Smith 1974) and is not expelled from the Kfs structure during any "intra-mineral differentiation." The formation of Ba-rich veins requires

the ingress of an external Ba-rich fluid at a later, post-emplacement stage, whose timing cannot be constrained by purely mineralogical arguments. The presence of discrete fluid pathways, the patchy textural relationship of the heterochemical Kfs generations, and the external addition of Ba are all independent arguments requiring a fluid circulation event post-dating the initial feldspar evolution by spinodal decomposition. The sericitization of plagioclase, adularization of Kfs, chloritization of biotite, and carbonate precipitation in fractures demonstrate that the CPP was a chemically open system during late-stage secondary fluid circulation event(s) and rules out that the Kfs only records processes that occurred in the first 10 ka after intrusion in a chemically closed system. This agrees with the observation that all geochronology-petrogenesis connections established on mineral geochronometers (e.g., Villa and Williams 2013) invariably document a significant diachronism between the establishment of primary petrogenesis and secondary retrogression reactions.

Mineral chemistry and imaging

The U–Pb community habitually examines the suitability of their specimens for analysis using preliminary screening at the whole-grain scale using relatively wide-angle fields of view, by CL (Gebauer et al. 1988) and/or BSE (Williams et al. 2007). These techniques reveal internal structures, heterogeneities, zoning, and inclusions of other minerals, in minerals deriving from a multi-stage petrogenesis that was not smoothed out by diffusive re-equilibration (Villa and Williams 2013). While monazite and zircon are routinely imaged, Kfs is usually not examined. In particular, no BSE, CL, or XPL textural characterization at the thin section scale is available for MH-10 (Lovera et al. 1993).

The structures revealed in CPP-02-01 using CL and BSE (Figs. 1, 2a, 3a) are curved and cut across pre-existing magmatic textures. They pertain to retrogression reactions during the sample's post-crystallization history with high a_{H2O} and variable X_{Ba}. They are in stark contrast with the CL structures imaged by Parsons and Lee (2009), which are euhedral and clearly pertain to a monotonic petrogenetic P–T-a–X path with constant X and very low a_{H2O}. An empirical correlation between CL emission variations and the concentration of Ba, Ca, K and Na is observed. The luminescence variations are likely not caused directly by the incorporation of Ba and Na, which are not thought to cause CL emission in materials based on their electronic configurations (Finch and Klein 1999). The observed correlation suggests that whatever element(s) enhances the luminescence was transported by the same external fluid infiltration that enriched Ba. As changes in chemical composition require mass transfer in a chemically open system, CL emission monitors both petrogenetic variations and the ingress of external fluids. The remainder of the grain shows a mixture of subtle, patchy CL variations. The question of the relevance of these variations to geochronology will be addressed below.

The Kfs-plagioclase interface is chevron shaped. This may indicate that the dissolution of Kfs and plagioclase occurs at different rates. The Kfs-albite interface appears to provide pathways for ingress of external fluids, as alteration (monitored by the Ba concentration, by CL hues, and/or by BSE brightness) is often seen to radiate from the interface into the pristine interior, achieving locally a complete substitution of the magmatic Kfs with a metasomatic, near end-member Kfs. In the following, these metasomatic replacement patches will be referred to as adularia (sensu Smith 1974, who emphasized the genetic process and the resulting chemical composition, rather than the crystallographic habit of euhedral specimens).

The EPMA analyses reveal chemical variations among traverses, but also within each of them. In the "pristine" grain containing traverse C–C′, 72 out of 87 points form a comparatively dense cluster with Ca/Na ratios between 0.007 and 0.053, 12 points have Ca/Na < 0.004, and 3 have Ca/Na > 0.062. This dense cluster has a median Ca/Na $= 0.028$. The distribution of the Ca/Na ratios is not Gaussian. This may be explained by assuming that the true Ca/Na ratio in the pristine ternary Kfs is actually close to 0.045 with a narrow variation range of 0.002; the shift to lower Ca/Na ratios could be due to minute alteration patches, much smaller than the spatial resolution of the EPMA beam (ca. 1 μm). In the following, a Ca/Na ratio of 0.007 will be considered as the very conservative cutoff between adularia replacement and pristine Kfs. In this assumption, traverse C–C′ contains 14 % adularia and 83 % pristine Kfs. The traverse A–A′ has 42 out of 60 points with Ca/Na < 0.007 and 12 points having Ca/Na between 0.007 and 0.053, i.e., consists of 70 % adularia and 20 % pristine Kfs. Traverse B–B′ contains 51 points with Kfs composition, 29 of which have Ca/Na < 0.007 and 22 have Ca/Na between 0.007 and 0.053 (57 % adularia, 43 % pristine Kfs). Thus, it is concluded that the analyzed grain separate contained at least 14 % adularia, probably closer to 25 % based on a visual estimate of the CL colors taken across the whole thin section. Traverse A–A′ contains 12 points whose cation sum per formula unit is <0.94, which is attributed to non-feldspathic alteration phases. Traverses B–B′ and C–C′ contain 1 and 2 such low cation sum points, respectively. All in all, these alteration phases account for a total of 7.6 % of the analyzed points.

The EPMA analyses show an even greater variability in the Ba concentration and the ratio of Ba to the major elements. None of the 270 EPMA analysis spots is simultaneously Ba-rich and Ca-rich, and Ba enrichment is only observed in zones that are depleted in Ca (Fig. 2e). A likely

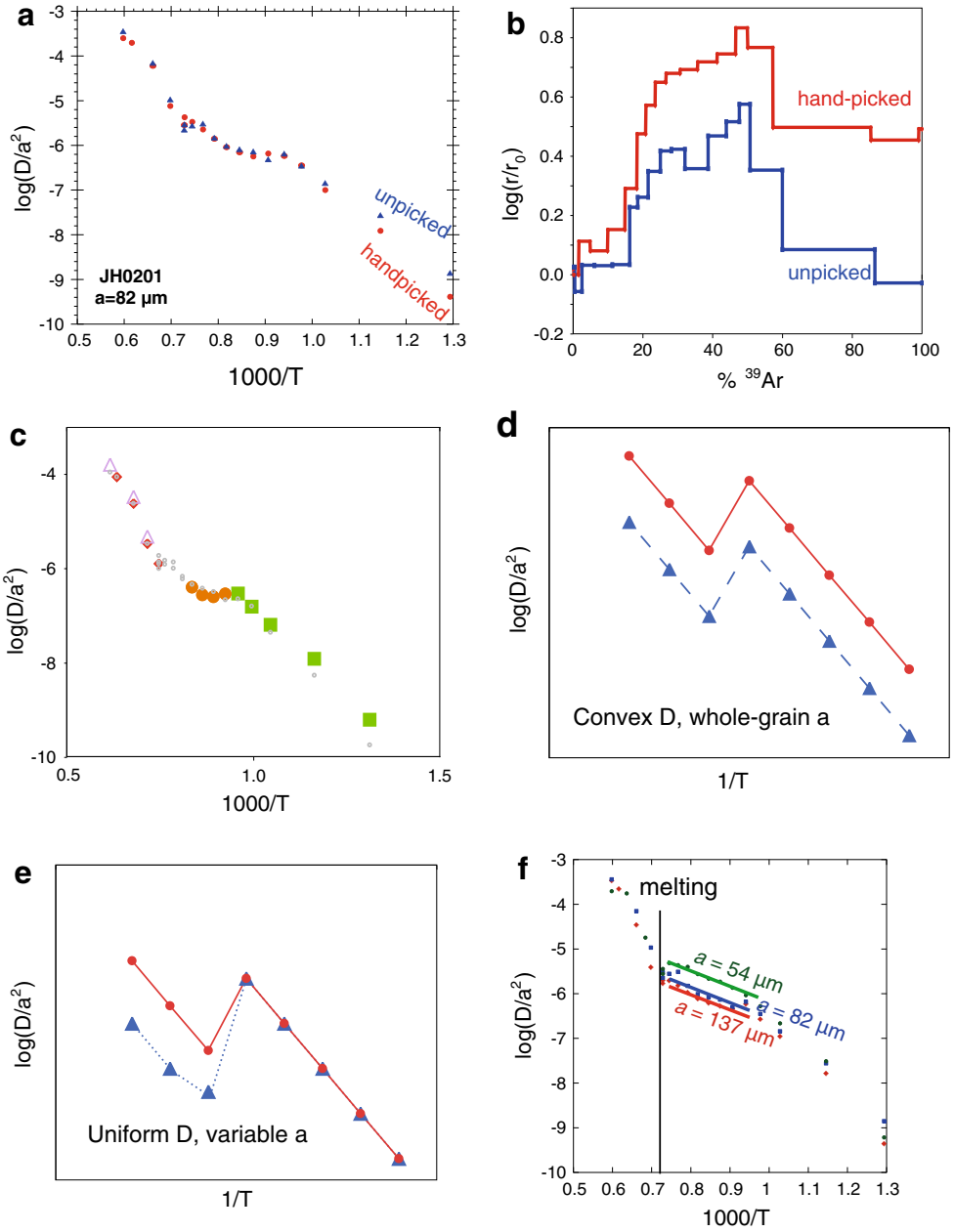

explanation is that CPP-02-01 records at least three fluid events separated in time as well as in fluid composition: a first fluid event formed porous adularia; a second fluid event exploited the previous pathways and introduced high Ba concentrations from outside; and a further event involving H_2CO_3. A textural connection to the carbonate-bearing veins is possible but not proven. Even if turbid areas are associated with porosity (Parsons and Lee 2009), the pores may not necessarily be interconnected (Norberg et al. 2013). However, these porous zones offer less resistance to dissolution when a subsequent fluid circulation event occurs and thus form a micro-aquifer while the pristine, less porous portions act as an aquitard. The connection between turbidity and chemical variations supports the use of CL imaging as an indicator of petrologic heterogeneity (Finch and Klein 1999).

Fitz Gerald and Harrison (1993) reported a narrow-angle TEM characterization, examining sample volumes of 1,000–5,000 µm^3 (*op cit*, p 376). The conclusion of the quest for the physical reality of the "domains" was "… No candidate exists for the intermediate domain boundaries" (*op cit*, p 377).

The TEM analyses of CPP-02-01 (Fig. 3) attempt to address two problems, which are apparently insoluble simultaneously: (1) assess whole-sample properties; (2) characterize petrogenetic processes at the 100 nm length

◀**Fig. 6** **a** Arrhenius plot for handpicked sieve fraction 82 μm (*circles*) and for the corresponding unpicked aliquot (*triangles*). The furnace temperature was not allowed to drop between heating steps (Huneke et al. 1969). The evident effect of handpicking is to reshape the Arrhenius trajectory at low temperature (see also Villa 2013). Since the triangles representing the low-temperature steps are shifted when impurity phases are manually removed, they do not pertain to D_{Kfs}, the degassing rate of Kfs sensu stricto. **b** Deviation from Arrhenian linearity (r/r_0 plot of Lovera et al. 1993) for the same sieve fraction. The change of apparent activation energy due to handpicking of impurities results in two very divergent trajectories. **c** Re-interpreted Arrhenius plot for the 82 μm sieve fraction from Fig. 6a. The effect of heterochemical phases is highlighted by the same color coding as Fig. 5b. *Large colored symbols* have a Ca/Cl/K signature near that of end-member phases; the in-between mixtures are shown as small gray points. The green squares at low temperature denote the Ar released from alteration phases. The brown circles denote adularia. The red diamonds denote the pristine magmatic Kfs. The open mauve triangles denotes the plagioclase. The gray points denote all those steps that reflect mixing between two or more fields in Fig. 5b. **d** Schematic prediction of Arrhenius trajectories for different sieve fractions of the same material. *Solid line*, trajectory of a fine-grained sieve fraction. If the nonlinearity is an intrinsic property of the diffusion coefficient D of the Kfs crystal structure (Villa 2013; Cassata and Renne 2013; Foland 1994), the Arrhenius trajectory of a coarser sieve fraction (*dashed line*) is parallel to the solid line; the vertical distance for all temperatures below melting is given by the ratio of the squares of the sieved grain sizes. **e** Schematic prediction of Arrhenius trajectories for different sieve fractions if the nonlinearity is the effect of a distribution of diffusion "domain" sizes superimposed on an intrinsically linear trajectory that results if D is viewed as the Fick's Law diffusion coefficient (Lovera et al. 1993). In this case, the larger sieve fraction contains exactly the same, sample-characteristic, "domain" size distribution as the smaller sieve fraction, with the possible addition of "domain" sizes larger than a_f, the grain size of the fine fraction. This model predicts that at the lowermost extraction temperatures, when only the smallest "domains" contribute significantly to the degassing rate, the two Arrhenius trajectories coincide, and start fanning out at high temperature (*dotted line*), if and when the hypothetical "domains" having $a > a_f$ contribute significantly to the degassing rate. **f** Arrhenius plots for the three unpicked sieve fractions. The parallelism of the three sieve fractions, when compared with the predictions in Figs. 6d, e, conclusively rules out the model in Fig. 6e and upholds the intrinsic nonlinearity of D instead

scale. However, by choosing two areas of contrasting petrographic appearance, the present work has provided answers to both problems.

Foil 1 shows a pristine region in Kfs; however, this alone does not guarantee that the bulk of the sample is as pristine as the analyzed foil. On the other hand, Foil 2 shows retrogression reactions. This alone implies with certainty that the sample is not pristine. Similar alteration microtextures had also been observed by Fitz Gerald and Harrison (1993, Fig. 7), yet their spatial extent was not discussed, and Lovera et al. (1993, p. 382) described the state of preservation of MH-10 as "remarkably pristine." In principle, because only a narrow field was accessible to the TEM analyses by Fitz Gerald and Harrison (1993), this could raise the question of how representative small-volume analyses actually are. However, the present study shows that the analysis of small-volume samples by TEM can be sufficient for an accurate conclusion, provided that regions representing all geochemical-petrological processes that affected the studied rock were sampled.

As a complementary support for the very labor-intensive, narrow-angle TEM analyses, the present study highlights the utility of whole-grain CL imaging in Kfs. The resolution of Kfs images mirrors that of zircon images. CL shows very clearly the replacement reaction(s) that result in a different distribution of color centers in the crystal. This may reflect both minor variations in chemical composition and variations in the average interatomic bond length/strength due to recrystallization under different P–T conditions. It is firmly established that microchemical and microtextural analyses of monazite and zircon relate chemical and chronological zonation and heterogeneities to metasomatic and metamorphic events (Villa and Williams 2013). Since the EPMA data demonstrate that the CPP-02-01 Kfs is chemically heterogeneous, it is important to constrain the relative timing of the replacement reactions and the isotopic closure.

In a similar problem setting, Grove and Harrison (1999) had initially proposed that the Th–Pb record of monazite was controlled by Pb diffusion to such a large extent that monazite could be modeled to yield thermochronometric information. Subsequent work (Williams et al. 2007) has demonstrated that the microstructural changes were due to recrystallization, whereby high-temperature Pb volume diffusion was negligible. The implication of Williams et al.'s (2007) work is to modify the cause–effect relationship: Pb was not lost "after/because of" the microstructural modification, but "while" recrystallization was going on, as incompatible Pb was selectively not incorporated into the newly forming monazite structure. The explanation of the link between the Ar isotope record and the CL-bright structures is similar. We propose that luminescence hues and Ar loss are two effects of the same cause, late-stage metasomatic fluid infiltration. This spawns the question if the sequence of reaction events forming these heterochemical phases is amenable to $^{40}Ar/^{39}Ar$ dating.

Age spectra and multi-isotope systematics

Villa and Hanchar (2013) provided evidence for two coexisting Kfs generations in samples from the Aar metagranite (Central Alps, Switzerland). Their origin is constrained through textural evidence for fluid interaction provided by CL and BSE imaging and EPMA. Just like in CPP, Villa and Hanchar (2013) linked anomalous Ba concentrations to fluid alteration, in areas with bright blue CL emissions, which led them to conclude that the

staircase-shaped age spectrum was caused by mixing between a young and an old Kfs generation (for which they proposed ages of ca. 10 and ca. 35 Ma, respectively). It is now clear that that insight is not an exceptional feature, which would make the Aar metagranite Kfs a regional curiosity. A phase mixture is observed to an even greater petrological complexity in the archetypal Kfs thermochronometer from the CPP. This implies that probably all Kfs samples, except perhaps those from young volcanic rocks that did not interact with any post-crystallization fluids, should be suspected by default to contain multiple, heterochemical, diachronous Kfs generations, unless detailed petrological investigations demonstrate the existence of individual exceptions on a case-by-case basis.

Age spectra alone often provide a clouded picture, as they focus on just the ^{39}Ar release and do not exploit the full potential of the ^{40}Ar/^{39}Ar technique. During irradiation, ^{37}Ar and ^{38}Ar are formed from Ca and Cl, respectively. The Ca/K and Cl/K ratios calculated from the artificial Ar isotope production are essential tools to diagnose mineral mixtures and to fingerprint their end-members (Villa et al. 2000). Especially valuable is the correlation between Ca/Cl/K ratios and the ^{40}Ar*/K ratio (i.e., the apparent step age), as it can help in dating the end-members of a mixture.

The Ar isotope data of the six Kfs aliquots from the CPP are chemically and chronologically diverse. The following phases can be fingerprinted by linking petrography with Ar isotope systematics: Fsp-0, a Ca-rich plagioclase removed by handpicking and containing "parentless" ^{40}Ar; Kfs-1, containing a large proportion of the sample's K budget, with moderate Ca/K; Kfs-2, a practically Ca–Cl-free Kfs; and one or more hydrous, Cl-rich, non-feldspathic alteration phase(s) that are also partly removed by handpicking. Kfs-1 is the most likely candidate for the magmatic Kfs, which is expected to contain small but nonzero amounts of Ca. The near-stoichiometric purity of Kfs-2 (close to Or_{100}) suggests it is adularia, although it should be pointed out that there is compositional overlap between adularia and what is typically referred to as microcline (*cf*. Deer et al. 1992, pp 414–415).

In addition to Kfs-1 and Kfs-2, the TEM photomicrographs have revealed a Ba-rich Kfs-3, whose small modal abundance may have obscured its clear detection in the Ar isotope record; future work might follow the approach by Hetherington and Villa (2007) and use Xe isotopes for additional fingerprinting.

Assigning apparent ages to Kfs-1 and Kfs-2 is possible in broad terms by making use of age-Cl/K and/or age-Ca/K correlation diagrams. The age of the Kfs-1 end-member ranges from 363.2 ± 0.5 to 359.7 ± 0.4 Ma in the coarsest and finest fraction, respectively. This 3.5 ± 0.6 Ma age difference might be due to diffusive loss of ^{40}Ar from the smaller grains. However, this is clearly not the only effect recorded by these samples, as the grain size fractions are not isochemical (both the total K concentration of the bulk samples, and the Cl/K and Ca/K ratios of the relevant steps, are different), i.e., the system records chemical mass transfer in addition to possible Ar loss from a fixed, homogeneous matrix. In the absence of documentation of *bona fide* bell-shaped diffusion profiles within Kfs grains, the option of diffusive Ar loss need not be further pursued, as other processes, such as the crystallization of late Kfs generations, predominate by far.

Adularia in CPP-02-01 is clearly a secondary replacement of the primary Kfs caused by interactions with hydrothermal fluids. It did not form during closed-system spinodal decomposition (following Parsons 1978), as it has a different chemical composition from the Kfs-1 generation and is not associated petrographically with unmixed plagioclase. The age of formation of adularia in CPP-02-01 is not constrained by the present data set. In principle, adularia could both have been formed at sufficiently low temperature that it mainly records its own growth, and at high temperature, such that its Ar record is solely controlled by diffusive Ar loss. To quantify the issue it would be necessary to separate pure adularia and determine its Ar diffusivity. This is not possible as long as the adularia breakdown is convoluted with that of other coexisting phases (see Fig. 6c below). In order to determine the diffusivity of ^{39}Ar in any mineral, that mineral must be present as a single, pure phase; multi-mineralic aggregates are not conducive to a reliable information, as disentangling an Arrhenius trajectory over several hundred °C is not possible without very accurate independent knowledge of the Arrhenius trajectories of each individual pure component and of the apportioning of ^{39}Ar to these components. Any model to mathematically separate orthoclase or microcline from plagioclase from adularia from clays in unknown modal proportions would contain a large number of unconstrained assumptions, making it arbitrary and untestable by external criteria.

Parsons et al. (1988, 1999) suggested that turbid Kfs has younger apparent ages than pristine areas in the same sample because it is inherently "leakier." However, it is not demonstrated that the pores are interconnected (Norberg et al. 2013) and thus represent no obvious microstructures of low Ar retentivity. We propose instead an analogy between the spatial pattern of Pb loss in monazite (see above) and that of Ar loss in Kfs, in that in both cases the loss of radiogenic isotopes should be viewed as the predominant effect of large-scale (>20 %) recrystallization in a chemically open system. To put the timing of Kfs replacement in a broader perspective, we can mention the Grimsel adularia (Hofmann et al. 2004), which is found in Pliocene low-temperature veins cutting the Hercynian Aar

granite. Between closed-system post-magmatic cooling of the granite and adularia formation by external fluids there was a time-lag of 300 Ma.

While it is not ruled out that diffusion could have caused some Ar loss from the adularia in CPP-02-01, it is not possible to quantify it. Both a protracted, late formation and diffusive losses act in the same direction, younging the K–Ar age of Kfs-2. Therefore, its temperature history remains unconstrained. So far, there are no reports constraining its formation temperature by fluid inclusion microthermometry (non-isotopic thermometry is necessary to avoid circular argumentations). In summary, adularia was formed at an unconstrained temperature by a replacement reaction in a chemically open system between the pluton's intrusion around 360 Ma and 310 Ma (the apparent age of the vertex with the lowest Ca/K ratio in the Ca/K-age correlation diagram). It is not known if adularia-forming reactions occurred continuously over an extended period or in discrete (single or recurrent) fluid circulation episode(s). A detailed discussion of metasomatism by hydrothermal fluids in northern Maine is a question of regional interest that is not resolved by one single sample from the CPP and would require an extensive geologic mapping and sampling campaign.

Finally, some datable retrogression phases suggest a later fluid circulation episode around 250 Ma, but as excess Ar is observed in many low-temperature phases, the most recent alteration event may have extended well into the Mesozoic. Clearly, in order to derive a regional geological history it is necessary to collect many ad hoc samples that can better constrain the late-stage water–rock interaction history.

Another unexpected feature of the age spectra is the observation that the low-temperature steps (the first 10 % of the ^{39}Ar release) of the finest handpicked aliquot have younger apparent ages than the corresponding step ages of the coarsest handpicked aliquot (Fig. 4d). This is impossible to reconcile with the suggestion that low-temperature steps are dominated by degassing of the smallest "domains." If the "Ar diffusion domains" were existing entities, albeit unobservable (Lovera et al. 1991, 1993), their properties should be robust irrespectively of the sieve size of the grains that host them, and the ages of initial heating steps should be indistinguishable for all sieve aliquots (irrespective of whether this apparent age is contaminated by excess Ar or not, it should be an intrinsic property of the smallest "domains" and should remain constant). Quite on the contrary, neither their apparent age nor their apparent Ar degassing rate is reproduced when different sieve fractions are compared (*cf.* Lovera et al. 1993; and the present study). This paradox is resolved by taking into account the Ca/Cl/K systematics, which reveals that the 54-μm aliquot, despite the handpicking efforts, still has a higher Cl concentration (Table S2), i.e., a higher modal abundance of Cl-rich young alteration phases than the 137 μm aliquot, and has therefore younger step ages.

A by-product of the identification of the outgassing phases by their Ca/Cl/K signature is constraining the mechanism by which a discordant age spectrum is produced. In the CPP-02-01 sample, the phases formed last are outgassed first; the most recent alterations precede the adularia, which is followed (with partial overlap) by magmatic Kfs, and finally by the phase with the oldest apparent age, restitic plagioclase. As the in vacuo degassing rate directly reflects the phase's interatomic bond length/strength (Villa 2006; 2013), the implication is that the metasomatic replacement phases formed later, at decreasing P–T, and also have a decreasing bond strength. The degassing sequence mirrors the P–T conditions of the respective replacement reactions along the rock's exhumation path.

The correlation between Ca/Cl/K signature and microtexture highlights critical problems in the interpretive context of ^{40}Ar/^{39}Ar data. Unlike isotope analysis in zircon, many ^{40}Ar/^{39}Ar studies report no petrologic characterization prior to analysis using advanced imaging and microchemical techniques. The lack of identification of petrogenetic heterogeneities and disequilibria questions the age interpretation of even apparently pristine samples, especially if they are based only on age spectra.

As replacement reactions are associated with characteristic microstructures, a question debated in the literature is whether the microstructural complexities caused the perturbation of the Ar isotope record or were subsequent to it. Harrison and Fitz Gerald (1986) and Fitz Gerald and Harrison (1993) propose the former, in the parallel cases of a heterochemical amphibole mixture and the MH-10 Kfs. However, the discussion by Onstott et al. (1995) demonstrated that the Ca/K systematics of the amphibole mixture contradicts a simple mass balance calculation and proposed that the laboratory release of Ar is qualitatively linked to "distinct decomposition temperatures" (a fact which was subsequently quantified by Villa et al. 2000). The study by Onstott et al. (1995) did not specifically address the Ar release mechanism in Kfs; it contradicted the proposition that microstructural complexities are the cause of age discordances. What emerges instead from the combination of their work with that by Villa et al. (2000) and the present work is that the principal cause of discordant age spectra are mineral replacement reactions. These reactions cause on one hand the loss of Ar during recrystallization, and on the other hand leave behind a mosaic of heterochemical phases. Thus, microstructural complexities are just another effect of the same process, retrograde reactions, that caused perturbation of the Ar isotope record. The laboratory Ar degassing rates of the retrogression phases are a function of

their chemical identity (Villa et al. 2000, Fig. 3). The degassing of Ar in the laboratory is not expected (Villa 2013) and not observed (this work, see below) to proceed from volume diffusion alone.

As each phase undergoes Ar degassing at different furnace temperatures (cf. Villa et al. 2000, Fig. 3a), phase diachronism can manifest itself as staircase-shaped age spectrum. When the furnace temperature intervals for Ar degassing of the coexisting phases are totally distinct (such as, e.g., biotite and hornblende in Villa et al. 1996) the mixture gives distinct plateaus, but if the degassing intervals partly overlap (as is the present case of the Kfs1–Kfs2 mixture) then a staircase results. There are many parallels between the present study and the work of Villa and Hanchar (2013), who demonstrated that staircase-shaped age spectra are observed in Kfs samples that contain a mixture of at least two distinct Kfs generations. The observations of staircase-shaped age spectra should be seen as analogous to discordant U–Pb analyses. In the early days of geochronology, "diffusionist" views led workers to interpret discordia lines as evidence of metamorphic Pb loss by diffusion (Tilton 1960). Subsequent insight emphasized the role of phase mixing as the vastly predominant cause of discordance (Mezger and Krogstad 1997).

In vacuo outgassing

The Arrhenius diagrams for the six sized aliquots of Kfs CPP-02-01 show the expected nonlinear trajectories. The following section will focus on the inter-sample and intra-sample variations of the trajectory. This can be done using two nearly equivalent presentations; the Arrhenius diagram itself, and the derived plot showing the deviations of the actual data from the modeled linear trajectory (called r/r_0 plot by Lovera et al. 1993 and Arrhenian nonlinearity plot by Villa 2013). The first comparison (Fig. 6a) is shown for sieve fraction 82 μm, between the handpicked (red circles) and the unpicked aliquot (blue triangles). The evident effect of the handpicking is to change the slope at low temperature, and more in general the shape, of the Arrhenius trajectory (see also Villa 2013). The open symbols at low temperature do not pertain to D_{Kfs}/a^2, the degassing rate of Kfs sensu stricto, because these points are shifted following manual removal of impurity phases. It is thus a mistake to estimate the Kfs activation energy for "domain" modeling from the degassing rate of a phase that is certainly not pure Kfs. The r/r_0 plot (Fig. 6b) is not exactly equivalent to the Arrhenius diagram in Fig. 6a, as it is based on a choice of E for the first three temperature steps; the r/r_0 plot more clearly visualizes the lack of robustness of the Arrhenius trajectory before and after handpicking. The presence of variable inventories of impurity phases is likely to have been the cause for the poor reproducibility of the r/r_0 plots obtained on the 850 μm aggregates analyzed by Lovera et al. (1993), as discussed in detail by Villa (2013).

We have shown above that the CPP-02-01 mineral separate analyzed consists of at least five heterochemical phases, empirically defined by isotope systematics and traceable to CL and BSE images and EPMA and analytical TEM microanalysis. As these five phases degas over different furnace temperature intervals, it is possible to visualize their contribution to the bulk degassing rate D/a^2 (Fig. 6c). It appears that a large part of the nonlinearity of the Arrhenius trajectory is accounted for by the superposed outgassing of two (or more) unrelated phases. In general, the superposition of five unrelated mineral structures having diverse outgassing rates gives a bulk degassing rate D/a^2 devoid of any profound meaning.

The role of grain sizes is illustrated in Fig. 6d, e, which depict two contrasting predictions for Arrhenius trajectories of different sieve fractions of the same material. The curvature around 750 °C has been explained in two mutually exclusive ways, which predict resolvably different trajectories. Explanation 1 maintains that the nonlinearity of the degassing rate D/a^2 as a function of $1/T$ is an intrinsic property of the diffusion coefficient D of the Kfs crystal structure (Villa 2013). This explanation predicts that the Arrhenius trajectory of the fine fraction (Fig. 6d, dashed line) be parallel to that of the coarse fraction (solid line); the vertical distance for all temperatures is given by the ratio of the squares of the effective Ar transport dimension. As shown by Foland and Xu (1990) the latter coincides with the physical grain size. In explanation 2, D is assumed to coincide with the Fick's Law diffusion coefficient, which follows an intrinsically linear trajectory; the observed nonlinearity is viewed as the effect of a variable "domain" size (Lovera et al. 1993). The larger sieve fraction contains exactly the same, sample-characteristic, "domain" size distribution as the smaller one, with the possible addition of "domain" sizes larger than a_f, the grain size of the fine fraction. This explanation predicts that at the lowermost extraction temperatures, when only the smallest "domains" contribute significantly to the degassing rate D/a^2, the two Arrhenius trajectories coincide (Fig. 6e), and start fanning out at high temperature, if there exist "domains" having $a > a_f$ that contribute significantly to the degassing rate (dotted line).

The observations (Fig. 6f) show that the three sieve sizes have parallel Arrhenius trajectories, which only overlap at temperatures higher than melting. Of special significance are the different procedures by which the sizing was achieved. In the present study, the samples were crushed one single time and then sieved, so that every aliquot was crushed for exactly the same duration; if

"domains" existed, each aliquot would be predicted to consist of identical random distributions of the same "domain" assemblage. In contrast, Lovera et al. (1993) used a sieved 850 μm grain diameter, and re-crushed some large grains to obtain smaller grains. They attributed the parallel Arrhenius trajectories to unexplained artifacts, which they proposed to have occurred during re-crushing (*op. cit.*, p. 390). In fact, the parallelism of Arrhenius trajectories is predicted by the interpretation proposed here, that most or all of the nonlinearity is inherent in D, and that the dependence on a is consistent with a being a constant equal to the sieve size. The presumed re-crushing artifact occurs in an identical way during single crushing; it is thus not an effect of crushing but it is directly tied to the whole-grain radius, independently of the number of disk mill iterations. The observation that different grain sizes of the CPP Kfs reproducibly exhibit parallel Arrhenius trajectories that contrast with the mathematical modeling by Lovera et al. (1993) should be viewed as proof that the Arrhenian curvature is an intrinsic property of D and that therefore there is no need for unobservable "domains" to explain the nonlinearity extrinsically.

Conclusions

1. Kfs from the CPP records open-system fluid infiltration, patchy metasomatic alteration, and retrograde replacement reactions. CL and BSE imaging reveal internal features that are quantified by EPMA as variations in the Ba and Na concentrations. At least five mineral species have been identified in the separates analyzed: a Ca-rich plagioclase and one (or more) hydrous, Cl-rich alteration phase(s) that are both partly removed by handpicking; and three Kfs generations, including magmatic Kfs, metasomatic adularia, and Ba-rich Kfs veins. Both the high Ba content and presence of adularia corroborate similar signs of reaction with hydrothermal fluids, such as sericitized plagioclase and chloritized biotite.
2. Staircase age spectra are the effect of the coexistence of multiple phases of different ages. Handpicking achieves mechanical removal of some of these phases and a corresponding modification of the shape of the age spectrum. It follows that age spectra are not an intrinsic, robust property of a mineral, but to a large extent the result of a mixture of heterochemical, diachronous phases.
3. The in vacuo release rate of the present CPP-02-01 Kfs sample reproduces the literature data on MH-10 and the nonlinearity of its Arrhenius trajectory. Multiple "domain" sizes would result in fanning Arrhenius trajectories that are not observed. The present study highlights that at least two effects contribute substantially to the nonlinearity of D: (1) the bulk ^{39}Ar degassing rate is a composite of the five unrelated degassing rates of the five phases observed in the mineral separate; (2) a priori arguments by two different approaches (Villa 2013; Cassata and Renne 2013) require that the degassing rate of the Kfs structure should exhibit a nonlinear Arrhenius trajectory due to structural rearrangements, which negates a fundamental assumption of Fick's Law, the inertness of the matrix.
4. The supposed strict identity of the physical process governing the staircase shape of age spectra and the nonlinearity of Arrhenius trajectories is not confirmed by the present study. Staircase-shaped age spectra of mineral separates are the effect of the coexistence of heterochemical phases having different apparent ages and are not a manifestation of Fick's Law. As neither the laboratory degassing nor the natural Ar inventory are exclusively a manifestation of volume diffusion, no mathematical model based on an inversion of laboratory degassing following Fick's Law can be upheld.
5. The principal geological information that may be extracted from the CPP Kfs pertains to the process that caused the observed metasomatic reactions, namely ingress of external hydrothermal fluids resulting in a chemically open system. It follows that if even the archetypal thermocronometer is a hygrochronometer dominated by phase multiplicity, it becomes mandatory to document the petrogenesis of every Kfs sample to be dated. Routine screening by CL and/or BSE, ideally followed by detailed chemical analyses by EPMA, should become as widespread in the K–Ar community as it deservedly is in the U–Pb community.

Acknowledgments The help of Dan Lux in retrieving the exact sampling location of MH-10 was decisive. Reviews by Ian Parsons and three anonymous referees, and the editorial comments by J. Hoefs were very helpful.

References

Arnold A, Jäger E (1965) Rb–Sr-Altersbestimmungen an Glimmern im Grenzbereich zwischen voralpinen Alterswerten und alpiner Verjüngung der Biotite. Ecl Geol Helv 58:367–390

Cassata WS, Renne PR (2013) Systematic variations of argon diffusion in feldspars and implications for thermochronometry. Geochim Cosmochim Acta 112:251–287

Chopin C, Maluski H (1980) 40Ar-39Ar dating of high pressure metamorphic micas from the Gran Paradiso area (Western Alps): evidence against the blocking temperature concept. Contrib Mineral Petrol 74:109–122

Cole DR, Ohmoto H, Lasaga AC (1983) Isotopic exchange in mineral-fluid systems. I: theoretical evaluation of oxygen isotopic exchange accompanying surface reactions and diffusion. Geochim Cosmochim Acta 47:1681–1693

Dahl PS (1997) A crystal-chemical basis for Pb retention and fission-track annealing systematics in U-bearing minerals, with implications for geochronology. Earth Planet Sci Lett 150:277–290

Deer WA, Howie RA, Zussman J (1992) An Introduction to rock forming minerals, 2nd edn. Longman Scientific and technical, New York 696 pp

Finch AA, Klein J (1999) The causes and petrological significance of cathodoluminescence emissions from alkali feldspars. Contrib Mineral Petrol 135:234–243

Fitz Gerald JD, Harrison TM (1993) Argon diffusion domains in K-feldspar I: microstructures in MH-10. Contrib Mineral Petrol 113:367–380

Fitz Gerald JD, Parsons I, Cayzer N (2006) Nanotunnels and pull-aparts: defects of exsolution lamellae in alkali feldspars. Am Mineral 91:772–783

Foland KA (1994) Argon diffusion in feldspars. In: Parsons I (ed) Feldspars and their reactions. Kluwer, Dordrecht, pp 415–447

Foland KA, Xu X (1990) Diffusion of ^{40}Ar and ^{39}Ar in irradiated orthoclase. Geochim Cosmochim Acta 54:3147–3158

Gebauer D, Quadt Av, Compston W, Williams IS, Grünenfelder M (1988) Archean zircons in a retrograded Caledonian eclogite of the Gotthard massif (Central Alps, Switzerland). Schweiz Mineral Petrog Mitt 68:485–490

Goldich SS (1938) A study in rock weathering. J Geol 46:17–58

Grove M, Harrison TM (1999) Monazite Th–Pb age depth profiling. Geology 27:487–490

Harrison TM, Fitz Gerald JD (1986) Exsolution in hornblende and its consequences for ^{40}Ar/^{39}Ar age spectra and closure temperature. Geochim Cosmochim Acta 50:247–253

Hart SR (1964) The petrology and isotopic-mineral age relations of a contact zone in the Front Range, Colorado. J Geol 72:493–525

Heizler MT, Lux DR, Decker ER (1988) The age and cooling history of the Chain of Ponds and Big Island Pond plutons and the Spider Lake Granite, west-central Maine and Quebec. Am J Sci 288:925–952

Hetherington CJ, Villa IM (2007) Barium silicates of the Berisal Complex, Switzerland: a study in geochronology and rare-gas release systematics. Geochim Cosmochim Acta 71:3336–3347

Hofmann BA, Helfer M, Diamond LW, Villa IM, Frei R, Eikenberg J (2004) Topography-driven hydrothermal breccia mineralization of Pliocene age at Grimsel Pass, Aar massif, Central Swiss Alps. Schweiz Mineral Petrog Mitt 84:271–302

Huneke JC, Smith SP (1976) The realities of recoil: ^{39}Ar recoil out of small grains and anomalous age patterns in ^{39}Ar-^{40}Ar dating. Proc Lunar Sci Conf 7:1987–2008

Huneke JC, Nyquist LE, Funk H, Köppel V, Signer P (1969) The thermal release of rare gases from separated minerals of the Mocs meteorite. In: Millman PM (ed) Meteorite research. Reidel, Dordrecht (NL)

Jäger E (1962) Rb-Sr age determinations on micas and total rocks from the Alps. J Geophys Res 67:5293–5306

Lasaga AC (1986) Metamorphic reaction rate laws and development of isograds. Mineral Mag 50:359–373

Lee MR, Parsons I (1997) Dislocation formation and albitization in alkali feldspars from the Shap granite. Am Mineral 82:557–570

Lee MR, Waldron KA, Parsons I (1995) Exsolution and alteration microtextures in alkali feldspar phenocrysts from the Shap granite. Mineral Mag 59:63–78

Leichmann J, Broska I, Zachovalova K (2003) Low-grade metamorphic alteration of feldspar minerals; a CL study. Terra Nova 15:104–108

Lovera OM, Richter FM, Harrison TM (1991) Diffusion domains determined by ^{39}Ar released during step heating. J Geophys Res 96:2057–2069

Lovera OM, Heizler MT, Harrison TM (1993) Argon diffusion domains in K-feldspar II: kinetic properties of MH-10. Contrib Mineral Petrol 113:381–393

Mezger K, Krogstad EJ (1997) Interpretation of discordant zircon ages: an evaluation. J Metamorph Geol 15:127–140

Norberg N, Harlov D, Neusser G, Wirth R, Rhede D, Morales L (2013) Experimental development of patch perthite from synthetic cryptoperthite: microstructural evolution and chemical re-equilibration. Am Mineral 98:1429–1441

Nyfeler D, Armbruster T, Villa IM (1998) Si, Al, Fe order-disorder in Fe-bearing K-feldspar from Madagascar and its implication to Ar diffusion. Schweiz Mineral Petrog Mitt 78:11–21

Onstott TC, Miller ML, Ewing RC, Arnold GW, Walsh DS (1995) Recoil refinements: implications for the ^{40}Ar/^{39}Ar dating technique. Geochim Cosmochim Acta 59:1821–1834

Parsons I (1978) Feldspars and fluids in cooling plutons. Mineral Mag 42:1–17

Parsons I, Lee MR (2009) Mutual replacement reactions in alkali feldspars I: microtextures and mechanisms. Contrib Mineral Petrol 157:641–661

Parsons I, Rex D, Guise P, Halliday A (1988) Argon-loss by alkali feldspars. Geochim Cosmochim Acta 52:1097–1112

Parsons I, Brown WL, Smith JV (1999) ^{40}Ar/^{39}Ar thermochronology using alkali feldspars: real thermal history or mathematical mirage of microtexture? Contrib Mineral Petrol 136:92–110

Parsons I, Magee C, Allen C, Shelley MJ, Lee MR (2009) Mutual replacement reactions in alkali feldspars II: trace element partitioning and geothermometry. Contrib Mineral Petrol 157:663–687

Parsons I, Fitz Gerald JD, Lee JKW, Ivanic T, Golla-Schindler U (2010) Time–temperature evolution of microtextures and contained fluids in a plutonic alkali feldspar during heating. Contrib Mineral Petrol 160:155–180

Parsons I, Fitz Gerald JD, Heizler MT, Heizler LL, Ivanic T, Lee MR (2013) Eight-phase alkali feldspars: low-temperature cryptoperthite, peristerite and multiple replacement reactions in the Klokken intrusion. Contrib Mineral Petrol 165:931–961

Smith JV (1974) Feldspar minerals. Springer, Heidelberg

Tilton GR (1960) Volume diffusion as a mechanism for discordant lead ages. J Geophys Res 65:2933–2945

Turner G (1988) Hydrothermal fluids and argon isotopes in quartz veins and cherts. Geochim Cosmochim Acta 52:1443–1448

Turner G, Huneke JC, Podosek FA, Wasserburg GJ (1971) ^{40}Ar–^{39}Ar ages and cosmic ray exposure age of Apollo 14 samples. Earth Planet Sci Lett 12:19–35

Villa IM (1997) Direct determination of ^{39}Ar recoil distance. Geochim Cosmochim Acta 61:689–691

Villa IM (2006) From the nm to the Mm: isotopes, atomic-scale processes, and continent-scale tectonic models. Lithos 87:155–173

Villa IM (2013) Ar diffusion in K-feldspar: present and absent. In: Jourdan F, Mark D, Verati C (eds) 40Ar/39Ar dating: from geochronology to thermochronology, from archaeology to planetary sciences. Geol Soc London Spec Pub 378:107–116. doi: 10.1144/SP378.4. First published online Jan 24, 2013

Villa IM, Hanchar JM (2013) K-feldspar hygrochronology. Geochim Cosmochim Acta 101:24–33

Villa IM, Williams ML (2013) Geochronology of metasomatic events. In: Harlov DE, Austrheim H (eds) Metasomatism and the chemical transformation of rock. Springer, Heidelberg, pp 171–202

Villa IM, Grobéty B, Kelley SP, Trigila R, Wieler R (1996) Assessing Ar transport paths and mechanisms for McClure Mountains Hornblende. Contrib Mineral Petrol 126:67–80

Villa IM, Hermann J, Müntener O, Trommsdorff V (2000) ^{39}Ar-^{40}Ar dating of multiply zoned amphibole generations (Malenco, Italian Alps). Contrib Mineral Petrol 140:363–381

Villa IM, Ruggieri G, Puxeddu M, Bertini G (2006) Geochronology and isotope transport systematics in a subsurface granite from the Larderello-Travale geothermal system (Italy). J Volcanol Geothermal Res 152:20–50

Waldron KA, Lee MR, Parsons I (1994) The microstructures of perthitic alkali feldspars revealed by hydrofluoric acid etching. Contrib Mineral Petrol 116:360–364

Wartho JA, Kelley SP, Brooker RA, Carroll MR, Villa IM, Lee MR (1999) Direct Ar diffusion measurements in a gem-quality Madagascar K-feldspar using the Ultra-Violet Laser Ablation Microprobe (UVLAMP). Earth Planet Sci Lett 170:141–153

Williams ML, Jercinovic MJ, Hetherington CJ (2007) Microprobe monazite geochronology: understanding geologic processes by integrating composition and chronology. Annu Rev Earth Planet Sci 35:137–175

Wirth R (2004) A novel technology for advanced application of micro- and nanoanalysis in geosciences and applied mineralogy. Eur J Mineral 16:863–876

Wirth R (2009) Focused ion beam (FIB) combined with SEM and TEM: advanced analytical tools for studies of chemical composition, microstructure and crystal structure in geomaterials on a nanometre scale. Chem Geol 261:217–229

Worden RH, Walker FDL, Parsons I, Brown WL (1990) Development of microporosity, diffusion channels and deuteric coarsening in perthitic alkali feldspars. Contrib Mineral Petrol 104:507–515